ELSEVIER

On the mechanistic origin of nanoscale "cold welding"

Peng Dong [a], Bo Song [a], Xin Zhai [a], Yanfei Gao [b,*]

[a] Department of Materials Science and Engineering, Taiyuan University of Technology, Taiyuan 030024, Shanxi Province, China
[b] Department of Materials Science and Engineering, University of Tennessee, Knoxville, TN 37996, USA

When nano-objects are brought together into contacts without any applied load at or near room temperature, a solid-state bonding can be accomplished either instantaneously or within some time, which has been termed by many recent works as "cold welding" as opposed to the traditional fusion welding. Such phenomena are more often encountered at nanoscale and have been utilized to build nano-devices such as nanowire-based interconnects or electrodes. Clearly, cold welding could be merely driven by the elastic adhesive contact, the analysis of which is straightforward but does not involve a time dependence. Room temperature, nanoscale, and contact size growth might suggest the operation of the curvature-driven sintering mechanism, or result from our proposed interfacial diffusional process in this paper as driven by a stress gradient (i.e., Coble creep). Here, we fabricated silver nanowires (AgNWs) with radius of several tens of nanometers, placed them into interconnect-like contacts, and measured the contact size growth at selected temperatures up to 200 °C. Out of the two hypothetical mechanisms (sintering versus Coble), only the latter mechanism can compare favorably with our experiments and result into physically meaningful parameters such as the activation energy and stress gradient magnitude. Consequently, this work presents the first conclusive study for nanoscale cold welding, as being the Coble diffusional creep.

Keywords: Nanoscale cold welding; Coble diffusional creep; Thermal activation

Introduction

Welding as an ancient processing technique has demonstrated great achievements in traditional and modern material applications, such as large structures (e.g., automotive and shipbuilding industries) and micro- and nano-electronics [1–4]. Especially for the latter applications, the race to create increasingly more integrated devices requires the development of various joining techniques at the nanoscale with industrial mass production rate. A quintessential example is the manufacturing of flexible transparent conductive electrodes, based on silver nanowire (AgNW) network, whereas direct contacts and intimate welding among individual AgNWs are utilized to establish a percolative conductive path for electronic transportation and also a reliable mechanical integrity for flexible needs [5,6]. Such novel applications pose daunting challenges for nanoscale welding, because of the need of creating and controlling highly localized temperature fields and the sensitivity to microstructural evolution at such small scales.

The above nano-manufacturing and nano-processing methods have motivated both scientific and technological communities to investigate a novel material-joining phenomenon. When nano-objects are brought together, they can suddenly bond together, which is termed as "cold welding" since this happens at room temperature [7–9]. Or more specifically, the spontaneous or delayed "welding" takes place at a homologous temperature that is usually $T/T_m << 0.5$ with T_m being the melting point. Should cold welding occur instantaneously, the underlying

* Corresponding author.
E-mail address: Gao, Y. (ygao7@utk.edu)

 https://doi.org/10.1016/j.mattod.2024.09.013

mechanism is most likely to be elastic adhesive contact (e.g., [7]), which can be combined with other mechanical processes such as imprinting, lifting, and delamination to fabricated integrated small devices. The theoretical analysis resembles the fracture mechanics, by considering the free energy minimization of elastic potential energy and surface energy. The comparison of these two energy terms gives a length scale, which explains why nanoscale features are required. This mechanism is also equivalent to crack healing; a macroscopic crack healing cannot be accomplished because the fractured surface of ductile materials is usually very rough. A recent work by Barr et al. [8] showed the healing of short fatigue crack in nanocrystalline Pt, exactly because of this "cold welding" mechanism being operated on the cleavage-like crack surface, despite the involvement of complex dislocation network to accommodate the cyclic deformation.

Lu et al. [9] reported nearly perfect welds formed between gold nanowires (AuNWs) with the same crystal orientation, strength and electrical conductivity as the rest of the parent wire, just within seconds by a butt-to-butt contact of AuNW pairs under room temperature. Their NWs are with diameters of about 10 nm, but the tip radius can be several times larger. While some of smaller wires show instantaneous welding, the larger ones exhibit a delayed process. Dislocation activities are usually very fast at such scales, and besides, no dislocations were observed in [9]. A time-dependent crack healing or cold welding can arise from time-dependent material properties (e.g., viscoelasticity) or from other kinetic processes such as the diffusion of low-affinity integrins on membranes of cell adhesion [10]. However, none of such mechanisms operates in the experiment of Lu et al. [9].

Different from the time scale of seconds in [9], AgNWs with diameters of several tens of nanometers in orthogonal contacts may require minutes or hours, or some sort of external heating above room temperature to realize the delayed welding process [6,11–13]. Garnett et al. [11] demonstrated the use of tungsten-halogen lamp illumination to successfully assemble AgNWs into large interconnected networks, thus named as light-induced plasmonic nano-welding. Many other heating methods have been developed to nanoscale processes, including laser heating, Joule heating, and electronic beam irradiation, which have demonstrated their efficacy in forming the desirable interconnects among NWs. It is explained in [11] that the localized heating originates from the localized surface plasmon resonance (LSPR) because there is a gap at the nanowire junction which enables effective light concentration and then forming a hot spot at the point. This gap arises from a polyvinylpyrrolidone (PVP) layer (~2 nm thickness) that usually remains on the surface of the nanowires after preparation. The PVP layer can be easily removed but still welding of NWs can be made at room temperature or heated by various ways to at most 200 °C [12,13]. Note that even the highest temperature is still at $0.35T_m$ of sliver in these works. Similar experiments have also been conducted to realize cold welding for many other types of materials and processing methods [14–16].

The mechanism responsible for the time-dependent nanoscale "cold welding" at or near room temperature (but far less than $0.5T_m$) without any applied load still remains elusive for the following two major reasons. First, the time dependence suggests the presence of some sort of thermally activated processes, so that feature size and temperature are naturally involved. Heated or not in the past experiments [9,11–13], there does not exist a quantitative and systematic measurement of the welding time versus the test temperature. The lack of such information prevents us from further investigating the controlling mechanism. Second, while many experiments seem to suggest a capillary-force-induced welding mechanism [12] (which is essentially the curvature-driven sintering mechanism [17]), a large contact size that is oftentimes instantaneously formed upon contact also suggests a large contribution from adhesive stress. From the energetic point of view, the driving force for mass transport is the gradient of chemical potential, and under both stress and curvature fields, the chemical potential along the arc length s can be written as [18,19]

$$\mu(s) = \mu_0 - \Omega(\sigma_n + \gamma_s\kappa) \quad (1)$$

where μ_0 is the reference value, Ω is the atomic volume, σ_n is the normal stress to the surface, γ_s is the surface energy (per unit area), and κ is the curvature (being negative if the surface is convex). In the classic sintering theory, σ_n is not present, so that the diffusional transport is from two contacting surfaces to the interface, as driven by the chemical potential difference, i.e., $-\gamma_s\kappa\Omega$. Note that if the nano-welding is a surface diffusion-controlled process, the height at the contact of crossed NWs will not change after welding. However, the obvious interpenetration at the junction of welded NWs [14–16] and our later results do not support the hypothesis. It is therefore reasonable to believe that the kinetic process is controlled by the interfacial diffusivity.

Due to the small size, the term of $\gamma_s\kappa$ might be on the order of gigapascal in the beginning, which is comparable to the adhesive stress level in σ_n. When the contact size grows and as will be shown later in this work, the curvature term is insignificant when compared to adhesive force. Therefore, it is hypothesized in this work that the nanoscale "cold welding" be controlled by the stress-driven mass transport, which is exactly the Coble diffusional creep. To verify our hypothesis, we have prepared AgNWs with diameters of several tens of nanometers and then vary the surrounding temperature so as to quantitatively determine the thermal activation processes. The comparison between curvature-driven sintering and Coble diffusional creep mechanisms will be emphasized in our following investigations.

Experimental observations

Silver nanowires were synthesized using the polyol process. First, 0.16 mM $CuCl_2{\cdot}2H_2O$ and 120 mM PVP were dissolved in 20 mL ethylene glycol (EG) and 160 mL EG, respectively. Then we add 80 mM $AgNO_3$, and heat the evenly mixed solution at 110 °C for 6 h. The synthesized product after cooling to room temperature was poured into 500 mL of acetone for rapid polycondensation, followed by washing with 200 mL of ethanol. This whole process was repeated three times. As will be characterized later, the prepared nanowires are crystalline and exhibit a fivefold twin structure, which is characteristic of silver nanowires prepared by the polyol method. The diameter of our AgNWs various within 30–60 nm, and their average length is about 50 μm. As shown in Fig. 1a, the AgNWs solution was dropped onto silicon wafers to produce random networks of AgNWs and dried naturally at

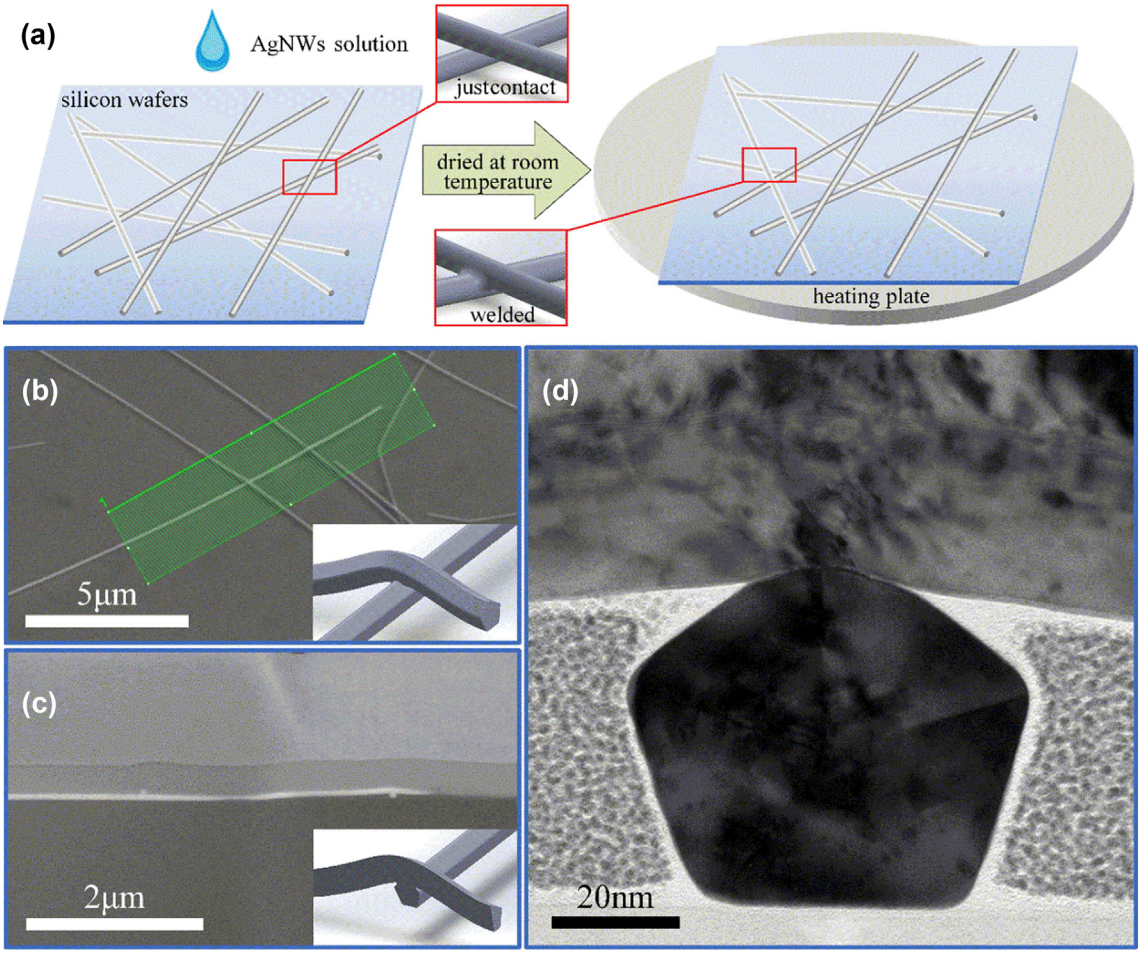

FIG. 1

Experimental details. (a) Drop the AgNWs solution onto silicon wafers to produce random networks of AgNWs. After dried naturally at room temperature, some samples were then placed on a heating plate for a specific period of time. (b) Selected area for the preparation of TEM specimens and vapor deposition of Pt protective cladding on its surface. (c) TEM thin-section specimens obtained by FIB preparation. (d) TEM image showing the cross section of the AgNW junction.

room temperature. While many AgNW contacts were already formed at this condition, some samples were subsequently heated on a heating plate with controlled temperature up to 200 °C for various time intervals, thus allowing us to observe the contact size growth at various temperatures.

Conventional scanning electron microscopy (SEM, FEI Strata 400S) was utilized to directly observe the cross-section samples of silver nanowire contacts. A carbon coating followed by a platinum coating was deposited prior to focused ion beam (FIB) milling in order to protect the AgNWs films from exposure to the gallium ion beam, which would otherwise amorphorize the structure, as shown in Fig. 1b–d. FIB was used to lift out from sample (cross-section of welded AgNWs), which was thinned down below 50 nm in thickness for characterizations under transmission electron microscopy (TEM, Talos F200S operated at 200 kV). Atomic force microscopy (AFM, Bruker Dimension Icon) was used to measure the three-dimensional topographic information of individual AgNW contacts.

Fig. 2a shows the tilted-view SEM images of crossed AgNWs after thermal annealing (20 min at 100 °C). It can be seen that the treated NWs are in close contact, and the surface of the NWs is slightly oxidized due to the longtime heat exposure. Furthermore, the height profiles measured by AFM show an interpenetration at the NW junctions, as shown in Fig. 2b. The AFM scans can be taken over various places, but only the top portion of the height profile can be used to fit the radius of curvature. Furthermore, given the radius information of two contacting NWs, we can then determine the contact size from the middle curve in Fig. 2b from a straightforward geometric relationship in Fig. 3. This indirect way of determining contact size is less accurate, compared to the direct observation under TEM as shown in Fig. 2c–e. These AgNWs exhibit a clear pentagonal cross-section [20]. For some of our nanowelds, the fast Fourier transformation (FFT) was carried out to confirm that the two NWs besides the interface have the same crystallographic orientations. Similar results have been reported in cold welding of single crystalline AuNWs by Lu et al. [9]. They believed the oriented-attachment mechanism was playing an important part during welding. In other words, once matching the orientation, welding will occur easily and rapidly. On the other hands, for some of our successful nanowelds, the two mating NWs can actually show different crystallographic orientations, while some unsuccessful

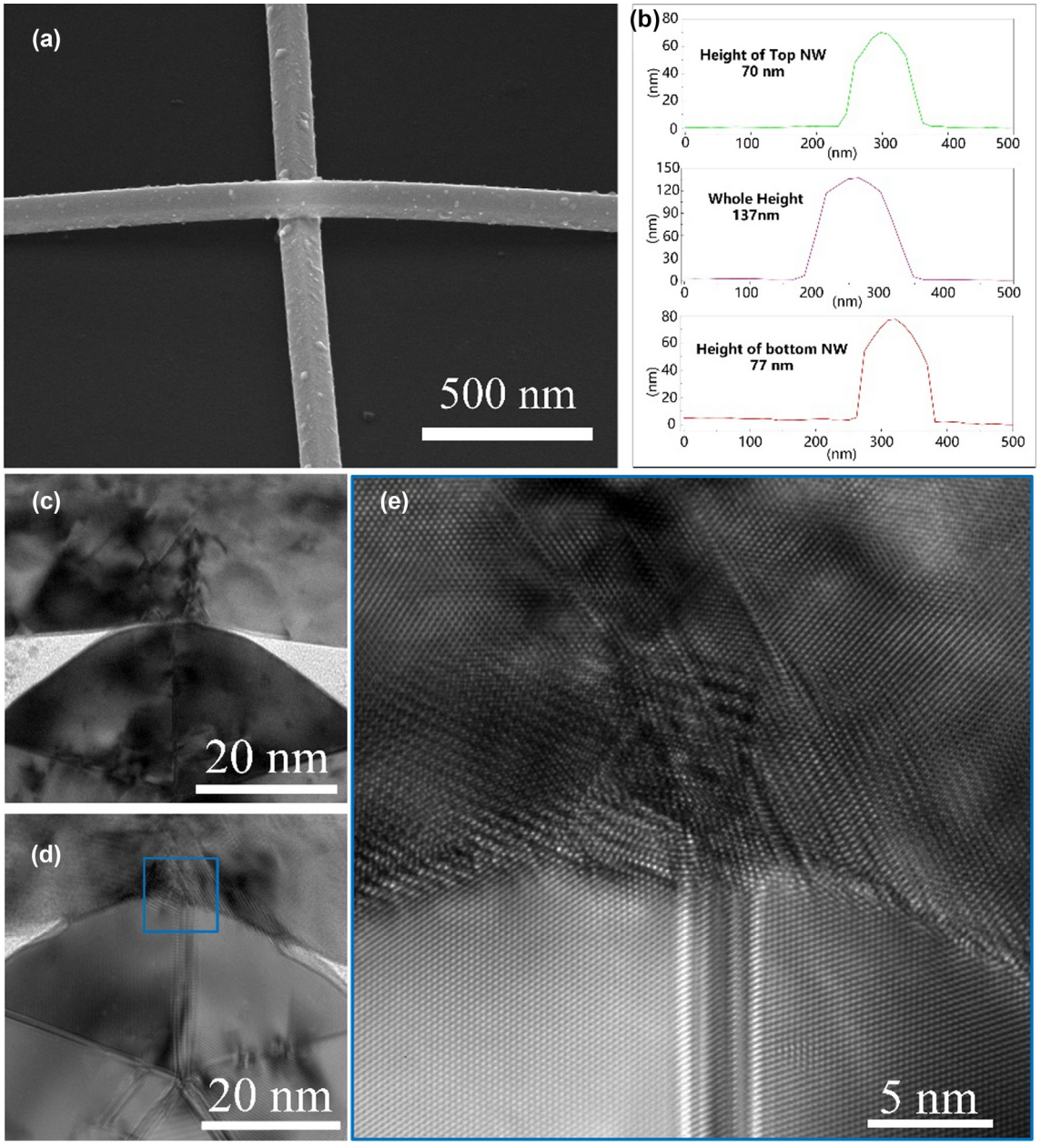

FIG. 2

The morphology of cold-welded AgNWs. (a) SEM of an orthogonal AgNWs junction after welding. (b) AFM-measured topography of the top NW (the green curve at the top), the bottom NW (the brown curve at the bottom), and the entire junction (the purple curve in the center). (c–e) TEM images showing the contact vicinity and the inverted V-shaped lattice defects (c, 3 h@50 °C; d, 600 s@100 °C; e, high magnification image of the box position in d).

welds could correspond to well aligned orientations (see an example in Supplement).

The contact size growth measurements at various temperatures were conducted by both AFM and TEM, although the latter is more accurate. The large collection of TEM images suggest that the pentagonal structure in AgNW does not change, and the contact may be accompanied by some peculiar dislocation structures such as the V-type one in Fig. 2e. But these findings are rare and the number of such dislocations is low. Therefore, it is believed that dislocation plasticity and crystallographic factors do not play a primary role in our nanowelds.

Theoretical analyses

In our theoretical investigation, the welding process of the NWs was treated as two consecutive problems, i.e., elastic adhesive contact between two orthogonally placed cylinders, followed by nanoweld growth at a given temperature. The former is an instantaneous process and therefore produces a finite contact size. The latter invokes a time-dependent mass transport process, which could be driven by curvature or stress gradient.

When two solids are placed in contact, the two free surfaces with surface energy γ_s will form an interface with interface

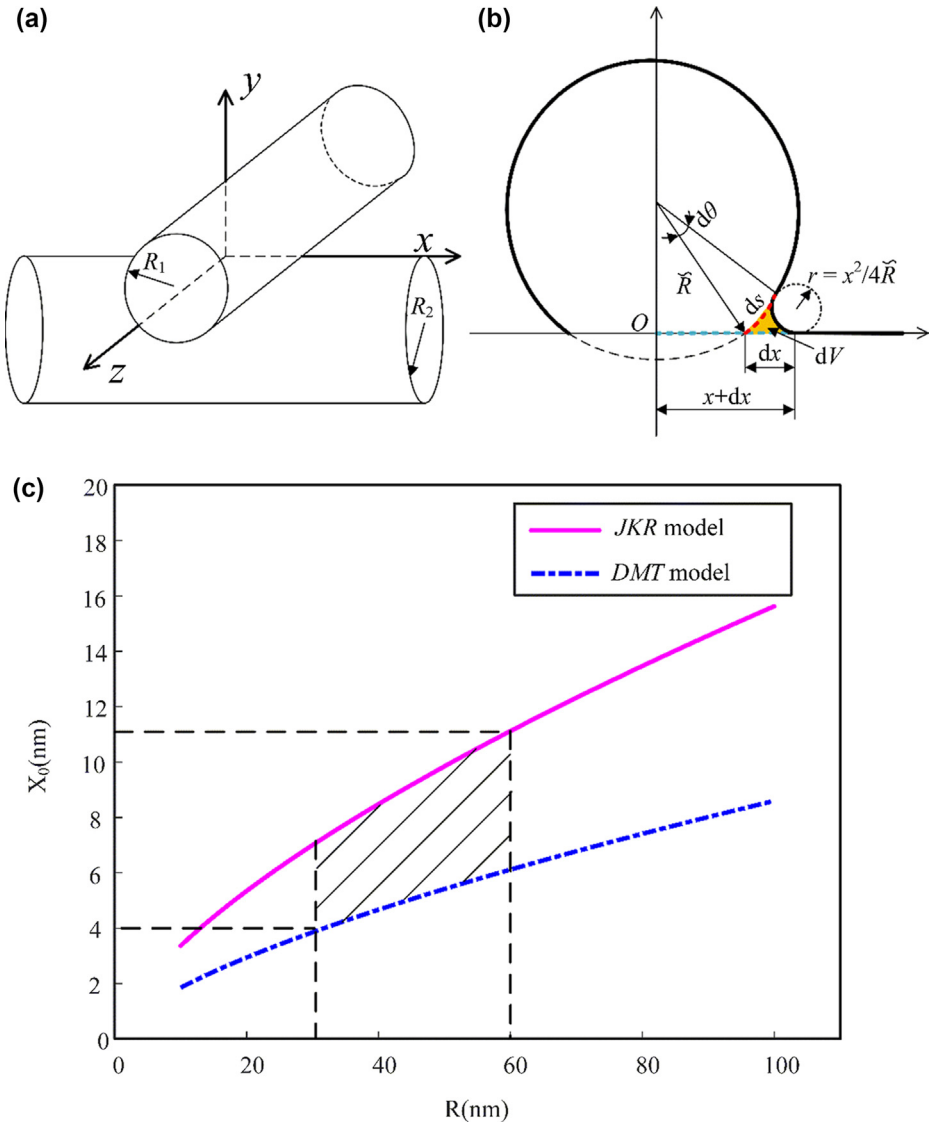

FIG. 3

Schematic diagram of the orthogonal contact of two NWs in (a), which is equivalent to an elastic sphere with composite radius on a rigid half-space in (b). The elastic adhesive contact gives an instantaneous contact size of X_0, as can be predicted from various contact models in (c).

energy γ_i, the difference of which is the work of separation of the two surfaces ϕ, given by

$$\gamma_i = 2\gamma_s - \phi \tag{2}$$

The half dihedral angle is determined from the Young-Dupré equation, $2\gamma_s \cos\theta = \gamma_i$. All these energy terms (energy per unit area, in fact) are on the order of 1 J/m^2 for metallic materials. The elastic contact analysis with the presence of adhesion can be conducted by using the linear elastic fracture mechanics (LEFM) method, leading to the Johnson-Kendall-Roberts (JKR) model [21]. The other limit solution by the Derjaguin-Muller-Toporov (DMT) model [22] takes no role of adhesion to the contribution of elastic deformation. The LEFM method assumes a mathematically perfect crack tip with stress singularities, which cannot be sustained in reality. Therefore, the work of adhesion can be replaced by a Dugdale model, which says that there is maximum tensile stress of σ_0 within a tensile separation range of δ_0 (outside of this value, there would be no adhesive interactions). Thus, $\phi = \sigma_0\delta_0$, where δ_0 can be interpreted as the characteristic separation length and is typically 0.5 nm, so that the adhesive stress magnitude, σ_0, is about 1 GPa. The use of Dugdale model will remove the stress singularity, and can bridge the JKR and DMT models as shown by Tabor [23] and Maugis [24].

Solutions for the elastic adhesive contact are well established. Here we are interested in the initial contact size X_0 as shown in Fig. 3b. Note that the contact of two orthogonal cylinders is equivalent to a sphere with radius $R_{eff} = \left(R_1^{-1} + R_2^{-1}\right)^{-1}$ in contact with a rigid half-space. The composite modulus is $E_{eff} = \left[\left(1-\nu_1^2\right)/E_1 + \left(1-\nu_2^2\right)/E_2\right]^2$, where E and ν are the Young's modulus and Poisson's ratio, respectively. Thus, the analytical solution gives

$$X_0 = \begin{cases} \left(9\pi R_{eff}^2 \phi / E_{eff}\right)^{1/3}, & \mu_{Tabor} > 1, \text{JKR } model \\ \left(1.5\pi R_{eff}^2 \phi / E_{eff}\right)^{1/3}, & \mu_{Tabor} < 0.1, \text{DMT } model \end{cases} \tag{3}$$

where the Tabor parameter, $\mu_{Tabor} = \left(\frac{R_{eff}\phi^2}{E_{eff}^2\delta_0^3}\right)^{1/3}$, dictates the transition between the two limit solutions. These results are plotted in Fig. 3c. In our case, Tabor parameter is calculated as about 0.77, meaning that X_0 should be located at the JKR-DMT transition region. The radius of nanowires in our experiments are about 30–60 nm, and it can be calculated that X_0 is in the range of 4.0–11.1 nm which is about 1/7 of the NW diameter. Obviously, when confronted with nanoscale welding, the initial neck size cannot be neglected.

Now for the mass transport analysis, we follow the classic sintering analysis (e.g., Rahaman [17]) but with the modification of stress term in the chemical potential as shown in Eq. (1). The diffusion flux from outside to the interface is

$$J_b = -\frac{D_b}{\Omega k_B T}\nabla\mu \approx \frac{D_b}{k_B T}\cdot\frac{\gamma_s\kappa + \sigma_{eff}}{X}, \tag{4}$$

where k_B is the Boltzmann constant. The gradient of chemical potential is approximated by the its difference over the contact. Right at the root of the contact edge, the curvature is approximated by $\kappa \approx 1/r = 4R_{eff}^2/X^2$ [17]. A more rigorous solution needs to be formulated to solve the boundary value problem of both adhesive contact and mass transport, which is out of the reasonable scope of this work. Thus, we adopt the above approximation and regard the effective stress σ_{eff} as close to σ_0 As shown in Fig. 3b, when the contact size grows, the volumetric mass transport dictates the following geometric relationship,

$$\frac{dV}{dt} = \frac{\pi X^3}{2R_{eff}}\cdot\frac{dX}{dt} = J_b 2\pi X\delta_b\Omega, \tag{5}$$

where the latter involves an interface thickness δ_b.

If we only consider the curvature-driven sintering process, the combination of Eqs. (3)–(5) gives the following relationship

$$\left.\frac{X - X_0}{R_{eff}}\right|_{\text{sintering}} = \left(\frac{96 D_b\delta_b\Omega}{k_B T}\frac{\gamma_s}{R_{eff}^4}t\right)^{1/6}. \tag{6}$$

On the other hand, if only the adhesive stress is considered to drive the mass transport along the interface (i.e., Coble diffusional creep), we have

$$\left.\frac{X - X_0}{R_{eff}}\right|_{\text{Coble}} = \left(\frac{16 D_b\delta_b\Omega}{k_B T}\frac{\sigma_{eff}}{R_{eff}^3}t\right)^{1/4}. \tag{7}$$

Naturally we can define two time scales,

$$\begin{cases} t_{reference}^{\text{sintering}} = \frac{k_B T}{96 D_b\delta_b\Omega}\cdot\frac{R_{eff}^4}{\gamma_s} \\ t_{reference}^{\text{Coble}} = \frac{k_B T}{16 D_b\delta_b\Omega}\cdot\frac{R_{eff}^3}{\sigma_{eff}} \end{cases} \tag{8}$$

Noting the thermally activation process of interface diffusion, we can write,

$$D_b\delta_b = (D_b\delta_b)_0 \exp\left(-\frac{Q_d}{R_g T}\right), \tag{9}$$

where R_g is the gas constant.

Experiment/model comparisons

Adhesion is ubiquitous in the contact of solids, and is especially so for nano-objects with high elastic moduli. It is important to notice that we cannot obtain an exact value of X_0 due to the sample preparation time. Our rough estimate from theoretical analyses in Eq. (3) can be our trial values at the beginning of our fitting process to be shown later. For micro-objects or larger ones, adhe-

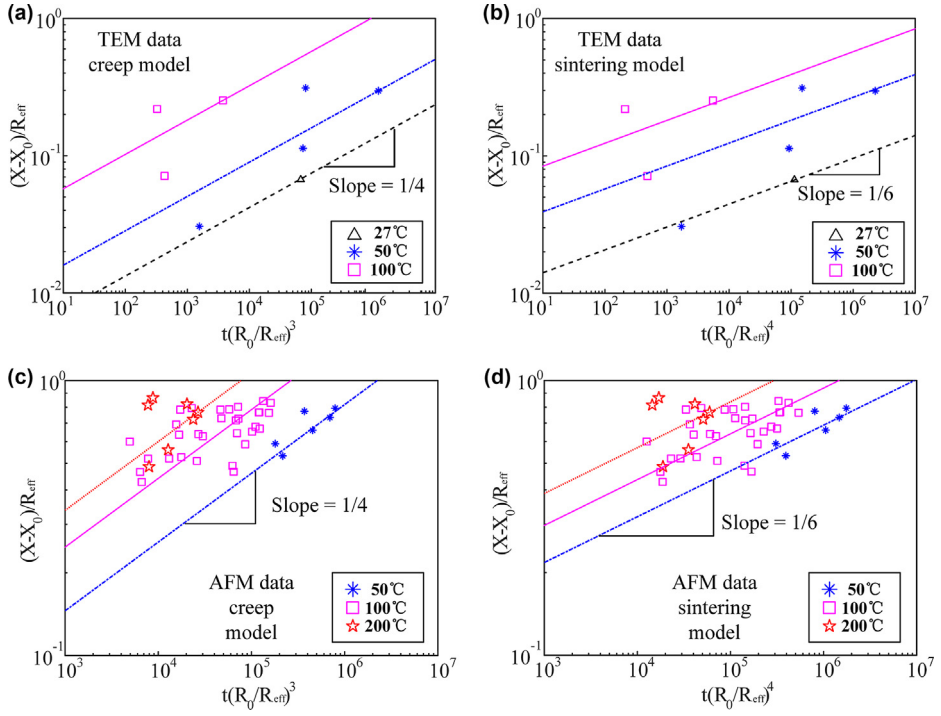

FIG. 4

The relationship between the growth of the normalized contact size and time (multiplied with different radius powers) by using either TEM or AFM measurements, and by comparing to either curvature-governed sintering model or our Coble diffusional creep model. See labels on individual plots. While fittings are generally acceptable in all these plots, only the Coble model gives the reasonable physical parameters.

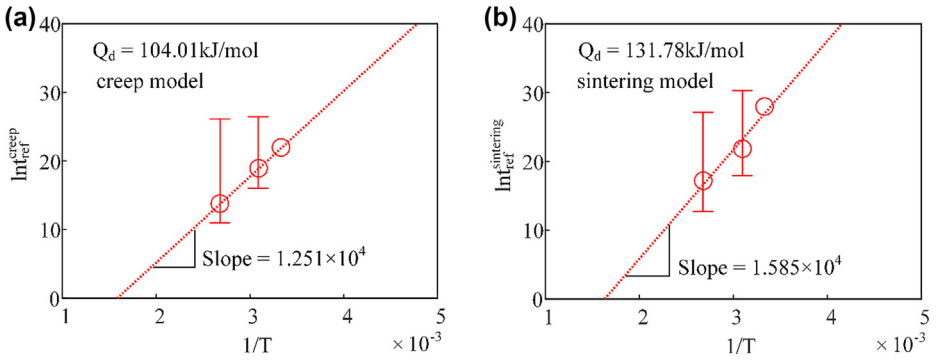

FIG. 5

Fitting the characteristic time (obtained from Fig. 4) to the reciprocal temperature gives the activation energy and stress magnitude in the Coble model (a), and the activation energy and surface energy in the sintering model (b).

sion has little contribution due to the length scale and also because surface roughness prevents a perfect contact. Therefore, bonding large objects should recourse to curvature-controlled sintering processes at elevated temperatures.

Our fitting results in Figs. 4 and 5 are based on the following procedure. The contact size X has been measured by both AFM and TEM with respect to heating temperature and heating time. From the consideration of experimental convenience and cost, there are far more AFM data than TEM data, while AFM data are less accurate. The initial contact size X_0 can be estimated and will also be adjusted in our fitting. There is a R_{eff} – dependence in our model, but the NW radius varies slightly. Therefore, we choose an average R_0 of all data, and then add a multiplicative factor of $(R_0/R_{eff})^3$ to time for Coble model or $(R_0/R_{eff})^4$ to time for sintering model. In the double logarithmic plots in Fig. 4, measurements at a given temperature should form a straight line with slope equal to 1/4 for Coble model or 1/6 for sintering model. Overall speaking, AFM data scatter more widely than TEM data, since AFM measurements were indirect and calculated the contact size from the NW junction height information. However, when comparing Coble and sintering models, their fittings are generally similar, although there is a slightly wider scatter in fitting to the sintering model. The slopes, on the other hand, can be successfully reproduced in all these four subplots.

From the fitted slopes in Fig. 4, we obtain the time scales with respect to the two models, as shown in Eq. (8). Then, plotting the logarithmic of this time scale with respect to the reciprocal temperature will allow us to fit the other parameters. As shown in Fig. 5, the slopes correspond to Q_d/R_g, and the intercept can be used to calculate either σ_{eff} or γ_s, depending which kinetic model is adopted. Under the assumption of sintering mechanism, the activation energy obtained is 131.78 kJ/mol, and the corresponding surface energy γ_s is about 416J/m^2, which is two orders of magnitude higher than the reasonable value. If Coble diffusion is the dominant mechanism, the corresponding activation energy is 104.01 kJ/mol, similar to the activation energy data for bulk silver (90 kJ/mol as shown by the data collection in Frost and Ashby [25]). Due to the huge scatter in Fig. 5a, the fitting result for the effective stress σ_{eff} is poor, but it is found to fall into the range of 0.2–0.5 GPa. This fitting result is nevertheless a very reasonable one. Using the JKR model, the contact edge will exhibit a tensile stress singularity. Although our problem usually falls in JKR-DMT transition region, there is still a high stress gradient at the contact edge with stress rising from compressive to a peak tensile stress of σ_0 and then to zero, if traversing from contact center to the edge. As explained before, a rigorous solution of boundary value problems that consider surface energy balance, force balance, and transient behavior of mass transport is not pursued here. Our model remains approximate, but our fitting results from Fig. 5 gives a value of σ_{eff} as $(1/4 - 1/2)\sigma_0$, suggesting the validity of our Coble diffusion model in understanding the cold welding phenomenon at nanoscales.

Summary

Nanoscale cold welding, referred to as the spontaneous bonding or gradual growth of the welding of nano-objects at or near room temperature, has drawn great attentions to many scientific and industrial investigators. It is straightforward to understand the instantaneous contact formation due to the adhesive forces between mating surfaces, but the delayed welding has only been suggested in literature to be a curvature-driven sintering process. However, there are only insufficient evidences to support this sintering model. This work creates hundreds of orthogonal contacts of AgNWs with radius of about 30–60 nm, and systematically measure the initial contact size and the contact size growth with respect to various heating temperatures (far below $0.5T_m$) and heating time. The time-dependent cold-welding measurements are compared to the classic curvature-driven sintering model and to our proposed Coble diffusional model along the interface as driven by the tensile stress at the contact edge. Fitting to the experimental data, it is clearly found out that curvature-driven (or capillary force) sintering mechanism is not responsible for nanoscale welding. This is the first study that clearly identifies the Coble diffusional creep be responsible for nanoscale "cold welding".

CRediT authorship contribution statement

Peng Dong: Writing – review & editing, Writing – original draft, Visualization, Validation, Supervision, Software, Resources, Project administration, Methodology, Investigation, Funding acquisition, Formal analysis, Data curation, Conceptualization. **Bo Song:** Writing – review & editing, Writing – original draft,

Visualization, Validation, Software, Resources, Project administration, Methodology, Investigation, Formal analysis, Data curation, Conceptualization. **Xin Zhai:** Writing – review & editing, Writing – original draft, Visualization, Validation, Software, Resources, Project administration, Methodology, Investigation, Formal analysis, Data curation, Conceptualization. **Yanfei Gao:** Writing – review & editing, Writing – original draft, Visualization, Validation, Supervision, Software, Resources, Project administration, Methodology, Investigation, Funding acquisition, Formal analysis, Data curation, Conceptualization.

Data availability

Data will be made available on request.

Declaration of competing interest

The authors declare that they have no known competing financial interests or personal relationships that could have appeared to influence the work reported in this paper.

Acknowledgements

PD, XZ, and BS acknowledge the financial supports from the Basic Application Research Project of Shanxi Province (No. 20210302123116). YG is grateful to the US National Science Foundation, Industry University Cooperative Research Center (I/UCRC) program, to the University of Tennessee under IIP 2052729.

Appendix A. Supplementary material

Supplementary material to this article can be found online at https://doi.org/10.1016/j.mattod.2024.09.013.

References

[1] M. Pouranvari, S.P.H. Marashi, Sci. Tech. Welding Joining 18 (2013) 361–403.
[2] P. Nautiyal et al., Carbon 122 (2017) 298–306.
[3] H.-J. Lee et al., ACS Appl. Mater. Interfaces 10 (2018) 14124–14131.
[4] M. Son, S. Jeong, D.-J. Jang, J. Phys. Chem. C 118 (2014) 5961–5967.
[5] D. Langley et al., Nanotechnology 24 (2013) 452001.
[6] X. Zhai et al., Nanotechnology 32 (2021) 505208.
[7] W.O. Akande et al., J. Appl. Phys. 107 (2010) 043519.
[8] C.M. Barr et al., Nature 620 (2023) 552–556.
[9] Y. Lu et al., Nature Nanotech. 5 (2010) 218–224.
[10] Z.W. Gao, Y.F. Gao, J. Mech. Phys. Solids 95 (2016) 557–574.
[11] E.C. Garnett et al., Nature Mater 11 (2012) 241–249.
[12] Y. Liu et al., Nano Lett. 17 (2017) 1090–1096.
[13] Y. Ge et al., J. Am. Chem. Soc. 140 (2018) 193–199.
[14] X. Zeng et al., ACS Appl. Mater. Interfaces 11 (2019) 37892–37900.
[15] J. Miao et al., Chem. Eng. J. 345 (2018) 260–270.
[16] K. Zhang et al., Nanoscale 10 (2018) 12981–12990.
[17] M.N. Rahaman, Sintering of Ceramics, CRC Press, 2007.
[18] J.S. Tello, A.F. Bower, J. Mech. Phys. Solids 56 (2008) 2727–2747.
[19] X. Wang et al., Materialia 21 (2022) 101350.
[20] H. Chen et al., J. Phys. Chem. B 108 (2004) 12038–12043.
[21] K.L. Johnson, K. Kendall, A.D. Roberts, Proc. R. Soc. Lond. A 324 (1971) 301–313.
[22] B.V. Derjaguin, V.M. Muller, Y.P. Toporov, Prog. Surf. Sci. 45 (1994) 131–143.
[23] D. Tabor, J. Colloid Interf. Sci. 58 (1977) 2–13.
[24] D. Maugis, J. Colloid Interf. Sci. 150 (1992) 243–269.
[25] H.J. Frost, M.F. Ashby, Deformation-Mechanism Maps: The Plasticity and Creep of Metals and Ceramics, Pegamon Press, 1982.